# Combining relativistic quantum-chemistry theories and electron-momentum spectroscopy to study valence-electron structures of molecules

K. Liu, C. G. Ning,* and J. K. Deng†

*Key Laboratory of Atomic and Molecular NanoSciences of MOE, Department of Physics, Tsinghua University, Beijing 100084, People's Republic of China*

(Received 22 April 2009; published 28 August 2009)

We report the combination of the Amsterdam density-functional relativistic quantum-chemistry program and electron-momentum spectroscopy to interpret electronic structures of molecules. We calculate momentum profiles of molecular orbital using the two-component relativistic theory. The momentum profiles of the complete valence shell orbitals of $I_2$ and $Au_2$ molecules are obtained in comparison between the nonrelativistic and relativistic calculations. The theoretical results show that relativistic effects have significant influences on the momentum distributions for valence orbitals of $I_2$ and $Au_2$. In order to verify the validity of the calculations, the high-resolution experimental momentum distributions of the $5P_{3/2}$ and $5P_{1/2}$ states of xenon are presented in comparison with relativistic quantum-chemistry theories.

DOI: 10.1103/PhysRevA.80.022716 PACS number(s): 34.80.Gs, 31.15.aj

## I. INTRODUCTION

Relativistic effects generally exist in high-$Z$ atoms and molecules containing high-$Z$ atoms. However, for a long time, it had been considered that it is not significant in the valence-electron structures of atoms and molecules since the valence electrons are well shielded from the nucleus and velocity of them is far less than the velocity of light [1]. It was not until the 1970s that scientists realized the importance of relativistic effects in the research of atoms and molecules. Relativistic effects principally include direct and indirect effects [2]. The direct relativistic effects may be divided into kinematical effects, which do not cause a splitting of energy levels due to the spin degrees of freedom, and into effects of spin-orbit coupling. Kinematical effects, which make the $s$ and $p$ atomic orbitals contract in the position space and energies of them decrease, are attributed to the high-speed movement of electrons in the vicinity of a heavy nucleus. For instance, the shrink of $1s$ orbital amounts to about 20% in mercury [3]. The spin-orbit coupling effects inducing the energy-level split are due to the coupling between spin and orbital angular momenta. The indirect relativistic effects, which are caused by the increased shielding of the nuclear charge due to the contracted inner-shell orbitals, make the $d$ and $f$ atomic orbitals extend in the position space and energies of them increase.

Molecules containing high-$Z$ atoms usually play important roles in functional materials, for example, using them as catalyzers. To understand the relativistic effects on chemistry, enormous progresses have been made on relativistic quantum chemical methods and calculations since 1980s [4–9]. Variational relativistic methods can be roughly divided into four-component, two-component, and one-component relativistic methods [10]. The relativistic quantum chemical calculations have been an important theoretical implement for studying high-$Z$ atoms and molecules containing high-$Z$ atoms.

Electron-momentum spectroscopy (EMS), based on the binary $(e,2e)$ ionization reaction, has been developed as a powerful and informative experimental tool for study of the electronic structure of atoms and molecules [11–13]. Although EMS, which can obtain both the orbital binding spectra and the electron-momentum profiles for each individual orbital, has been used to investigate relativistic effects for many years [14–19], the applications were mainly limited to the heavy atomic targets due to the complexity of relativistic effects in a molecular target. We report momentum profiles of molecular orbitals using two-component relativistic calculations.

In this work, we combine the powerful EMS technique and the current relativistic quantum-chemistry computations. We anticipate that this combination will provide an accurate testing method for the relativistic computational methods. An interface program is coded for reading the required information of electronic wave functions, and then these data are used to generate the momentum distributions for each orbital through our newly developed NEMS program [20]. The brief methodological introduction is presented first, and then the various theoretical momentum distributions of Xe $5P_{3/2}$ and $5P_{1/2}$ states are compared with our high-resolution experimental $(e,2e)$ measurements in order to verify the validity of theoretical methods we employed. And then, the relativistic and nonrelativistic calculations for momentum profiles of valence shell orbitals of $I_2$ and $Au_2$ are reported. The calculated results show that the relativistic effects have significant influences on the momentum profiles of the valence shell electrons of molecules containing high-$Z$ atoms.

## II. THEORETICAL AND EXPERIMENTAL DETAILS

In the symmetric noncoplanar $(e,2e)$ experiment, the target molecules are ionized by a electron beam with a high enough energy, and two outgoing electrons have the same kinetic energies and the same polar angles $\theta$ ($\theta_1=\theta_2=45°$) relative to the incoming electron beam. The momenta of electrons prior to being knocked out can be determined

*ningcg@tsinghua.edu.cn
†djk-dmp@tsinghua.edu.cn

 

through the out-of-plane azimuthal angle $\phi$ between the two outgoing electrons by the formula

$$p = \left[ (2p_1 \cos\theta - p_0)^2 + 4p_1^2 \sin^2\theta \sin^2\left(\frac{\phi}{2}\right) \right]^{1/2}, \quad (1)$$

where $p_1$ and $p_2$ ($p_1 = p_2$) are the magnitudes of the momentum of each of the two outgoing electrons and $p_0$ is the momentum of the incident electron. Under the conditions of high impact energy, high-momentum transfer, and negligible kinetic-energy transfer to residual ion, the plane-wave impulse approximation (PWIA) gives a good description for the collision. Under the PWIA, the EMS differential cross section for randomly oriented gas-phase molecules is given by [11]

$$\sigma_{EMS} \propto \int \frac{d\Omega}{4\pi} |\langle e^{-ipr} \Psi_f^{N-1} | \Psi_i^N \rangle|^2, \quad (2)$$

where $e^{-ipr}$ is the plane wave for electrons. $|\Psi_f^{N-1}\rangle$ and $|\Psi_i^N\rangle$ are the total electronic wave functions for the final ion state and the target molecule ground (initial) state, respectively. The $\int d\Omega$ indicates the spherical average due to the randomly oriented gas-phase target. Using the target Kohn-Sham approximation (TKSA) of density-functional theory (DFT) [21], Eq. (2) is greatly simplified by

$$\sigma_{EMS} \propto \int d\Omega |\psi_j^{KS}(p)|^2, \quad (3)$$

where $\psi_j^{KS}(p)$ is the momentum space Kohn-Sham orbital for the $j$th electron. The integral in Eq. (3) is known as the spherically averaged single electron-momentum distribution. To this extent EMS has the ability to image the electron density of individual "orbitals" selected according to their binding energies.

The details of the EMS spectrometer used in this work have been previously reported elsewhere [22]. It employs a symmetric noncoplanar geometry and uses a double toroidal energy analyzer and position sensitive detectors to achieve the energy and angle multichannel detections. To achieve higher resolution both in energies and electron momenta, significant modifications have been implemented on the spectrometer. In brief, an electron gun equipped with an oxide cathode, which worked at much lower temperature than the generic filament cathodes, was used to generate the electron beam with low-energy spread and small divergence angle. The passing energy was set to 50 eV from 100 eV for increasing energy resolution. Since the oxide cathode is easily poisoned by active gas, an additional vacuum chamber was especially designed to mount the electron gun. This chamber is evacuated to a base pressure of $10^{-7}$ Pa by a 600 L/s molecular turbo pump, with a hole of 2 mm in diameter connecting to the main chamber. Owing to these measures and optimization of electron optics using the Monte Carlo simulation, the angle resolutions, $\Delta\varphi = \pm 0.84°$ and $\Delta\theta = \pm 0.53°$, were obtained through the standard calibration run for argon. In the present work, the energy resolution, which highly depends on the emitting current of the cathode due to the space effects, was $\Delta E = 0.65$ eV [full width at half maximum (FWHM)] through controlling the emitting current.

The nonrelativistic and relativistic calculation methods used in present work were performed using DFT along with the standard hybrid Becke 3-Parameter Lee Yang and Parr (B3LYP) [23] functional by means of the Amsterdam density-functional (ADF) 2007 program [9,24,25], which can perform relativistic and nonrelativistic calculations for atoms and molecules. The relativistic calculations include scalar relativistic and spin-orbit relativistic methods. The latter is one kind of two-component relativistic methods which can provide spin-orbit splitting components. The scalar and spin-orbit relativistic methods are incorporated via the zero-order regular approximation (ZORA) [26]. The nonrelativistic calculations used triple-zeta with one polarization (TZP) function basis sets, while the relativistic calculations including scalar and spin-orbit relativistic calculations used ZORA/triple-zeta with two polarization (TZ2P) function basis sets. The optimized geometries of $I_2$ and $Au_2$ were used for all the calculation.

The ADF program constructs the electronic wave function using the fragmental molecular-orbital [9] and the double group representation [27,28] with the Slater-type basis sets. The calculation of electron-momentum profiles needs Fourier transforms and spherical averaging due to the randomly molecular orientations in the gas phase. Therefore, we developed a program named ADFCOVT, which was coded using FORTRAN90 to handle the scalar and the spin-orbit relativistic electronic wave functions of the molecules, and the extracted information was used as the input file for the NEMS program, which is capable of computing spherical averaged electron-momentum distributions and handling the atomic basis functions in a general analytic way, no matter what is their quantum number for the angular momentum and which type (Gaussian or Slater) of basis sets they are. The molecular orbital generated using the spin-orbit relativistic ADF calculation has the following form:

$$\Psi(r) = \Psi_\alpha(r)\alpha + \Psi_\beta(r)\beta, \quad (4)$$

where $\alpha$ and $\beta$ are the spin variables and orthogonal with each other. $\Psi_\alpha(r)$ and $\Psi_\beta(r)$ are the space wave-function components for the spins $\alpha$ and $\beta$, respectively. The momentum distributions $|\Psi(p)|^2$ for the two-component molecular orbitals are given by

$$|\Psi(p)|^2 = |\Psi_\alpha(p)|^2 + |\Psi_\beta(p)|^2, \quad (5)$$

where $|\Psi_\alpha(p)|^2$ and $|\Psi_\beta(p)|^2$ are the momentum distributions of for the spin $\alpha$ and $\beta$ components.

## III. RESULTS AND DISCUSSION

### A. Experimental and theoretical studies on Xe 5*p* orbitals

The binding energy spectrum of xenon summed over all azimuthal angles in the range of 8–34 eV at impact energies of 1200 eV plus binding energies are illustrated in Fig. 1. It can be seen that the $5P_{3/2}$ (12.13 eV) and $5P_{1/2}$ (13.44 eV) states are well separated with the energy resolution $\Delta E = 0.65$ eV, which is much better than previous work $\Delta E = 1.6$ eV by Cook *et al.* [14]. The peaks located at the higher binding energies mainly consist of the 5*S* state and its satel-

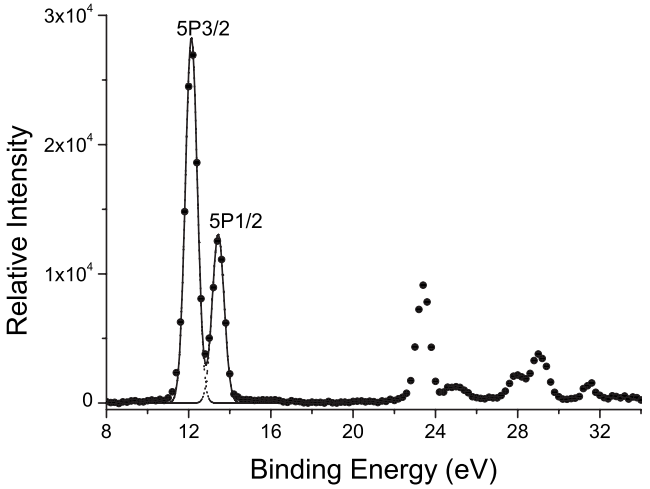


FIG. 1. Binding energy spectra of xenon at the impact energy of 1200 eV.

lite lines. The detailed assignment for these peaks can be found in Ref. [15]. In order to obtain the experimental momentum distributions for state $5P_{3/2}$ and $5P_{1/2}$ individually, the binding-energy spectra at different azimuthal angles are fitted with two Gaussian peaks in the region of 8–16 eV. Each Gaussian peak is represented by dashed lines, while their sum, the overall fitted spectrum is indicated by the solid line. Since the extracted experimental momentum distributions are in the relative scale, here we compare the ratio of $5P_{3/2}-5P_{1/2}$ with the theoretical calculations to avoid the uncertainty of normalizations. The experimental cross-section ratios of $5P_{3/2}-5P_{1/2}$ obtained by this work and previous work [14] at impact energy 1200 eV are compared with different theoretical ratios in Fig. 2. It can seen that the nonrelativistic calculation (thin dash line 4) predicted a constant ratio of 2, totally insensitive to the momentum $p$, which is inconsistent with the experimental ratios. However, all relativistic calculations can well describe the experimental ratios as the function of the momentum $p$. The curve 1 is our PWIA calculation using relativistic DFT-B3LYP method, and the distorted-wave impulse approximation (DWIA) (curves 2) and PWIA calculations using relativistic Hatree-Fock (HF) [or Dirac-Fock (DF), curve 3] method are taken from the work of Cook *et al.* [15]. The agreement between our PWIA calculations and previous PWIA work (curves 1 and 3) indicated the correctness and feasibility of our theoretical calculations. The theoretical momentum distribution of $5P_{1/2}$ within PWIA has a zero point at $p=2.15$ a.u., and therefore PWIA ratio curve has a singularity at that point. PWIA calculations as well as DWIA describe the experimental ratio quite well in the low-momentum region $p<1.0$ a.u. However, in the high-momentum region $p>1.2$ a.u., the DWIA calculation gives a better description of experimental results than PWIA. It should be noted that the relativistic DWIA calculation of Cook *et al.* [15] was at the impact energy of 1000 eV and hence would show more distorted effects than expected at the higher energy of 1200 eV.

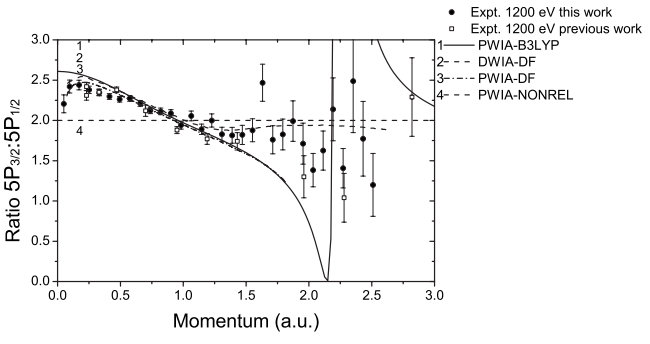


FIG. 2. Cross-section ratios of xenon $5P_{3/2}-5P_{1/2}$ measured at the impact energy of 1200 eV in present work and previous work in comparison with theoretical calculations (1) present PWIA work using B3LYP relativistic method, (2) DWIA using DF method from Ref. [15], (3) PWIA using DF method from Ref. [15], and (4) PWIA using nonrelativistic calculations.

### B. Relativistic effects in $I_2$

The iodine molecule $I_2$ has $D_{\infty h}$ point-group symmetry and its electronic configuration in the ground state with single group representations can be written as

$$(\text{core})^{92}(2\sigma_g)^2(2\sigma_u)^2(3\sigma_g)^2(2\pi_u)^4(2\pi_g)^4.$$

With the double group symmetry using in spin-orbit relativistic ADF calculations, its electronic configuration in the ground state can be written as

$$(\text{core})^{92}(15J_g^{1/2})^2(15J_u^{1/2})^2(16J_g^{1/2})^2(16J_u^{1/2})^2$$
$$(8J_u^{3/2})^2(17J_g^{1/2})^2(8J_g^{3/2})^2.$$

In the ground state, the 14 electrons are arranged in five orbitals of $D_{\infty h}$ point group and seven orbitals of double group, respectively.

The binding energies of each valence orbital are shown in Table I. Single group orbitals $2\sigma_g$, $2\sigma_u$, and $3\sigma_g$ are corresponding with double group orbitals $15J_g^{1/2}$, $15J_u^{1/2}$, and $16J_g^{1/2}$, respectively. The single group orbitals $2\pi_u$ and $2\pi_g$ are split into two double group orbitals $16J_u^{1/2}$, $8J_u^{3/2}$, $17J_g^{1/2}$, and $8J_g^{3/2}$ due to the relativistic effects (see Table II).

The inner valence orbitals $2\sigma_g$ and $2\sigma_u$ are formed by $5s$ atomic orbitals of iodine atom, and other orbitals $3\sigma_g$, $2\pi_u$, and $2\pi_g$ are formed by $5p$ atomic orbitals of iodine atom. Compared with previous photoelectron spectrum (PES) work [29–31], the binding energies calculated by spin-orbit relativistic method all underestimate the respective experimental binding energies by ~2.6–2.8 eV, which is due to the fact that $X_c$ functionals in DFT calculations fail to give the correct dispersion interaction in the large $r$ region [32].

In Fig. 3, the momentum profiles using nonrelativistic, scalar relativistic, and spin-orbit relativistic methods are compared for the orbitals $2\sigma_g$, $2\sigma_u$, $3\sigma_g$, $2\pi_u$, and $2\pi_g$. The scalar relativistic and spin-orbit relativistic calculations generate the same momentum distributions for the orbitals $2\sigma_g$, $2\sigma_u$, and $3\sigma_g$ except that the nonrelativistic calculations have stronger intensity in the low-momentum region. The scalar relativistic and spin-orbit relativistic calculations predict a stronger intensity than nonrelativistic calculations in the high-momentum range for these orbitals. These phenomena

TABLE I. Binding energies (eV) of the valence orbitals of $I_2$.

| | Nonrelativistic | Scalar relativistic | Spin-orbit relativistic (two-component relativistic) | | PES (Refs. [29–31]) |
|---|---|---|---|---|---|
| $2\sigma_g$ | −19.631 | −20.412 | $15J_g^{1/2}$ | −20.376 | |
| $2\sigma_u$ | −16.535 | −17.977 | $15J_u^{1/2}$ | −17.942 | |
| $3\sigma_g$ | −10.469 | −10.244 | $16J_g^{1/2}$ | −10.336 | 12.94 |
| | | | $16J_u^{1/2}$ | −9.095 | 11.81 |
| $2\pi_u$ | −8.944 | −8.706 | $8J_u^{3/2}$ | −8.397 | 11.01 |
| | | | $17J_g^{1/2}$ | −7.264 | 9.983 |
| $2\pi_g$ | −7.119 | −6.983 | $8J_g^{3/2}$ | −6.627 | 9.356 |

can be explained with the reason that the constriction of $5s$ and $5p$ atomic orbitals of iodine atom in position space due to the relativistic effects results in the constriction of $2\sigma_g$, $2\sigma_u$, and $3\sigma_g$ orbitals of $I_2$ molecule, and therefore these orbitals are more extensive and dispersive in momentum space.

The spin-orbital interactions remove the degeneration of $2\pi_u$ and $2\pi_g$ orbitals. The momentum distributions of the $16J_u^{1/2}$ and $8J_u^{3/2}$ split from the $2\pi_u$ orbital are illustrated in Fig. 3(d). The differences of momentum profiles among nonrelativistic, scalar relativistic calculation for $2\pi_u$, and the sum of spin-orbit relativistic calculations for $8J_u^{3/2}$ and $16J_u^{1/2}$ are slight. It is interesting to note that the spin-orbit relativistic calculations predicted a higher intensity for $8J_u^{3/2}$ than for $16J_u^{1/2}$ in the low-momentum region. There is a similar phenomenon for the $2\pi_g$ orbital in Fig. 3(e). However, the spin-orbit relativistic calculations predicted a noticeable intensity for $17J_g^{1/2}$ in the low-momentum region of $p<0.25$ a.u. It is a quite exceptional result because the nonrelativistic and the scalar relativistic calculations, as well as the two-component relativistic calculation for $8J_g^{3/2}$, predict zero intensity at the momentum origin. This can be explained in that the $17J_g^{1/2}$ orbital not only is split from the $2\pi_g$ orbital but also have some components from the $3\sigma_g$ orbital, which has a maximum intensity at the momentum origin (see Table II). The high-resolution EMS experiments should be able to provide a test for this result.

In order to distinguish the differences between $8J_u^{3/2}$ and $16J_u^{1/2}$ and $8J_g^{3/2}$ and $17J_g^{1/2}$ more clearly, the branching ratios of $8J_u^{3/2}$ to $16J_u^{1/2}$, $8J_g^{3/2}$ to $17J_g^{1/2}$ are shown in Fig. 4. Nonrelativistic theory suggests that the branching ratios are independent of the momentum and equal to 1. However, the branching ratios derived from the spin-orbit relativistic calculations deviate from the value of 1. We find that the intensity for $16J_u^{1/2}$ is smaller than for $8J_u^{3/2}$ in the momentum region $p<0.9$ a.u. and greater in the momentum region $p>0.9$ a.u.; the intensity for $17J_g^{1/2}$ is greater than for $8J_g^{3/2}$ in the region $p<0.2$ a.u. and $p>0.95$ a.u. and smaller in the momentum region 0.2 a.u. $<p<0.95$ a.u. The theoretical studies [2] demonstrate that the intensity of momentum distribution for a large total angular momentum $j$ in the low-momentum region is greater than that for small $j$ component, and the case is inversed in high-momentum region due to the relativistic effects. Our calculated results are consistent with the theoretical predictions [2].

### C. Relativistic effects in $Au_2$

The gold molecule $Au_2$ contains 158 electrons and has $D_{\infty h}$ point-group symmetry. Its ground-state electronic con-

TABLE II. The percentage (%) of single group orbital in the double group orbital representation for $I_2$ and $Au_2$.

| | | | | | | |
|---|---|---|---|---|---|---|
| | | | $I_2$ | | | |
| $15J_g^{1/2}$ | $15J_u^{1/2}$ | $16J_g^{1/2}$ | $16J_u^{1/2}$ | $8J_u^{3/2}$ | $17J_g^{1/2}$ | $8J_g^{3/2}$ |
| $2\sigma_g$ (99) | $2\sigma_u$ (100) | $3\sigma_g$ (96.78) | $2\pi_u$ (98.42) | $2\pi_u$ (99.94) | $3\sigma_g$ (3.13) | $2\pi_g$ (99.94) |
| | | $2\pi_g$ (3.10) | | | $2\pi_g$ (96.72) | |
| | | | $Au_2$ | | | |
| $20J_g^{1/2}$ | $20J_u^{1/2}$ | $11J_u^{3/2}$ | $11J_g^{3/2}$ | $12J_u^{3/2}$ | $21J_g^{1/2}$ | $5J_g^{5/2}$ |
| $4\sigma_g$ (92.16) | $3\pi_u$ (90.56) | $3\pi_u$ (64.96) | $2\delta_g$ (88.78) | $3\pi_u$ (34.98) | $4\sigma_g$ (7.12) | $2\delta_g$ (99.92) |
| $3\pi_g$ (7.64) | $4\sigma_u$ (9.17) | $2\delta_u$ (34.94) | $3\pi_g$ (11.06) | $2\delta_u$ (64.94) | $3\pi_g$ (79.8) | |
| $5\sigma_g$ (0.06) | | | | | $5\sigma_g$ (12.94) | |
| $5J_u^{5/2}$ | $21J_u^{1/2}$ | $12J_g^{3/2}$ | $22J_g^{1/2}$ | | | |
| $2\delta_u$ (99.94) | $3\pi_u$ (9.16) | $2\delta_g$ (11.08) | $4\sigma_g$ (1.18) | | | |
| | $4\sigma_u$ (90.64) | $3\pi_g$ (88.84) | $3\pi_g$ (12.4) | | | |
| | | | $5\sigma_g$ (86.98) | | | |

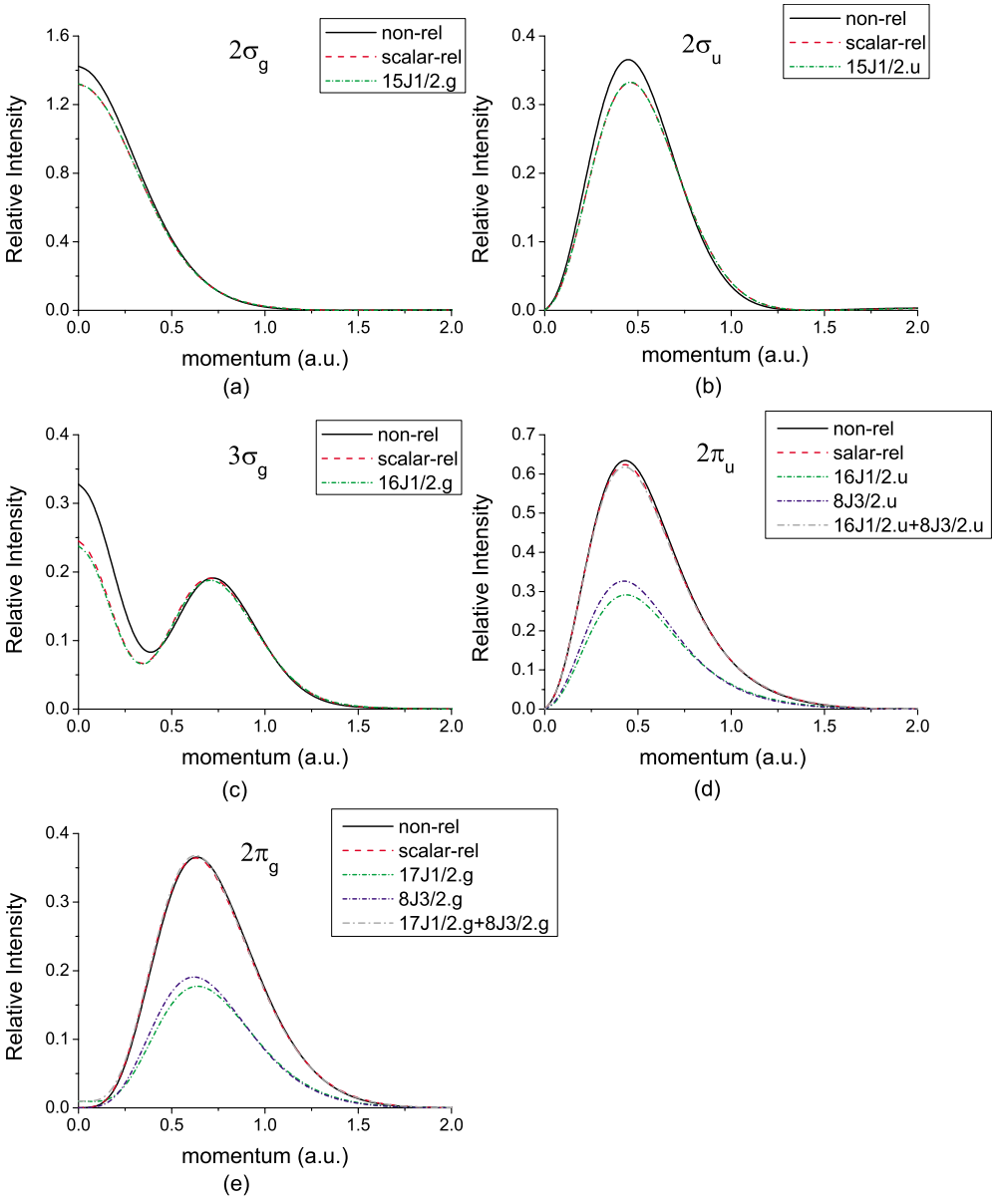


FIG. 3. (Color online) The spherically averaged momentum profiles for valence orbitals of $I_2$.

figuration with single group representations can be expressed as

$$(\text{core})^{136}(4\sigma_g)^2(3\pi_u)^4(2\delta_g)^4(2\delta_u)^4(3\pi_g)^4(4\sigma_u)^2(5\sigma_g)^2.$$

With double group symmetry using in spin-orbit relativistic ADF calculations, its electronic configuration in the ground state can be written as

$$(\text{core})^{136}(20J_g^{1/2})^2(20J_u^{1/2})^2(11J_u^{3/2})^2(11J_g^{3/2})^2(12J_u^{3/2})^2$$

$$(21J_g^{1/2})^2(5J_g^{5/2})^2(5J_u^{5/2})^2(21J_u^{1/2})^2(12J_g^{3/2})^2(22J_g^{1/2})^2.$$

Figure 5 illustrates the huge differences between energy levels of $Au_2$ using three different methods and complicated interactions between single group and double group orbitals because gold exhibits very strong relativistic effects. The thickness of lines between electronic structures using scalar relativistic method and spin-orbit relativistic method denote the intensity of the interactions, which means percentages of single group orbitals in double group orbitals.

The percentages of single group orbital in the double group orbital representation for $I_2$ and $Au_2$ are listed in Table II. Only the main single group orbital components (more than 0.05%) are listed in the table due to the space limit. It can be easily seen that one double group orbital corresponds to or is split from one single group orbital (the percentage is more than 96%) for $I_2$. However, it is quite different for $Au_2$ because of complicated single group orbital components in one double group orbital representation. One double group orbital cannot be simply ascribed to the split from one single group orbital. For example, the double group orbital $21J_g^{1/2}$ has three main single group orbital components: $4\sigma_g(7.12\%)+3\pi_g(79.8\%)+5\sigma_g(12.94\%)$.

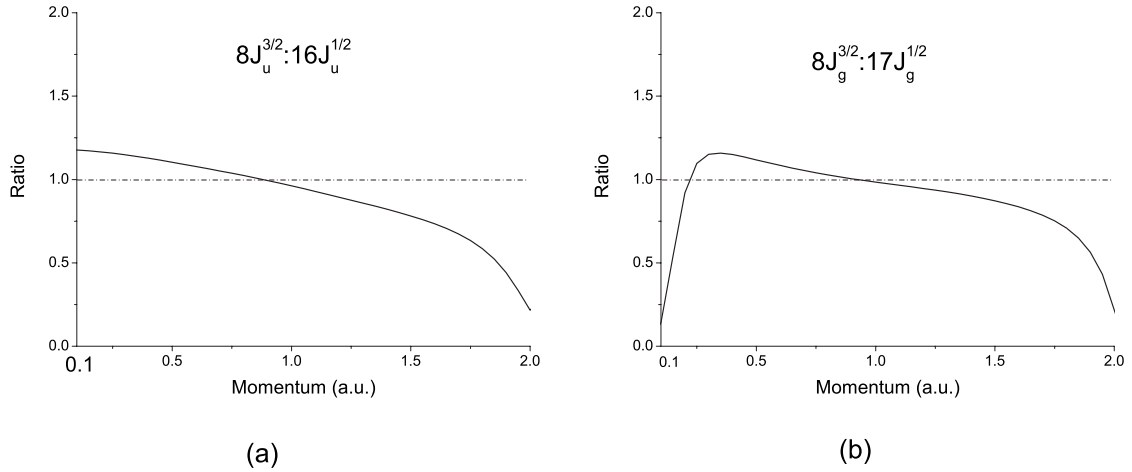


FIG. 4. The ratio of (a) $8J_u^{3/2}-16J_u^{1/2}$ (b) $8J_g^{3/2}-17J_g^{1/2}$ as a function of momentum for $I_2$.

The atomic electronic structure of gold atom features a filled $5d$ shell and a singly occupied $6s$ shell, i.e., $5d^{10}6s^1$, and $5\sigma_g$ orbital of $Au_2$ consists of two $6s$ orbitals of gold atom, and other outer valence orbitals of $Au_2$ consist of $5d$ orbitals of gold atom. Based on these facts, the binding energy of $5\sigma_g$ orbital using nonrelativistic method is significantly higher than that using scalar relativistic method and inversely for other outer valence orbitals since relativistic effects make the energy of $s$ orbital lower and $d$ orbital higher. Table III shows the binding energies of each valence orbitals of $Au_2$.

There is no one-to-one correspondence between the double group orbital and single group orbital. Therefore we cannot simply consider one double group orbital corresponds to or is split from one single group orbital for $Au_2$. Here, for convenience of comparing, we roughly choose the greatest single group orbital component as the generating orbital for each double group orbital.

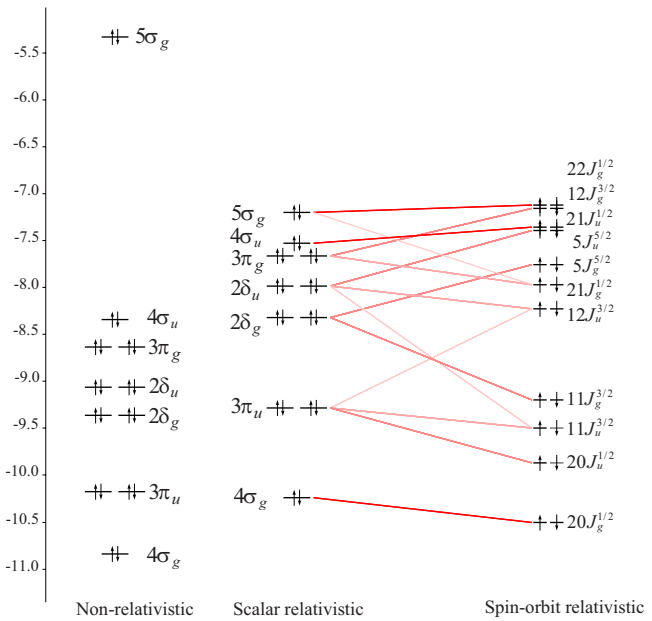


FIG. 5. (Color online) Binding-energy levels of $Au_2$ using nonrelativistic, scalar relativistic, and spin-orbit relativistic calculations and interactions between single group orbitals and double group orbitals.

The momentum profiles of valence orbitals of $Au_2$ are plotted in Figs. 6(a)–6(g). The most inner valence orbital $4\sigma_g$ reveals the remarkable relativistic effects in Fig. 6(a). In the momentum region $p<1.0$ a.u., the relative intensity using nonrelativistic method is lower than that of the scalar relativistic methods, which indicates that the $4\sigma_g$ orbital of $Au_2$ expands in position space under the relativistic condition. The discrepancy of momentum profiles between $4\sigma_g$ of scalar relativistic method and $20J_g^{1/2}$ of spin-orbit relativistic method results from the various components in the orbital $20J_g^{1/2}$ (see Table II).

Similarly, the shift and concentration toward the low-momentum region under relativistic condition appears in Figs. 6(b)–6(f), suggesting that the $3\pi_u$, $2\delta_g$, $2\delta_u$, $3\pi_g$, and $4\sigma_u$ orbitals expand in position space. The different distribution between single group orbitals of scalar relativistic method and the sum of double group orbitals of spin-orbit relativistic method due to the various components in double group orbitals (see Table II). Especially, the $21J_g^{1/2}$ orbital consists of 12.94% $5\sigma_g$, 79.80% $3\pi_g$, and 7.12% $4\sigma_g$. There-

TABLE III. Binding energies (eV) of the valence orbitals of $Au_2$ with three methods.

| | Nonrelativistic | Scalar relativistic | Spin-orbit relativistic | |
|---|---|---|---|---|
| $4\sigma_g$ | −10.840 | −10.239 | $20J_g^{1/2}$ | −10.500 |
| $3\pi_u$ | −10.177 | −9.284 | $20J_u^{1/2}$ | −9.863 |
| $2\delta_g$ | −9.361 | −8.316 | $11J_u^{3/2}$ | −9.492 |
| $2\delta_u$ | −9.059 | −7.983 | $11J_g^{3/2}$ | −9.196 |
| $3\pi_g$ | −8.635 | −7.664 | $12J_u^{3/2}$ | −8.227 |
| $4\sigma_u$ | −8.341 | −7.526 | $21J_g^{1/2}$ | −7.970 |
| $5\sigma_g$ | −5.333 | −7.200 | $5J_g^{5/2}$ | −7.758 |
| | | | $5J_u^{5/2}$ | −7.394 |
| | | | $21J_u^{1/2}$ | −7.355 |
| | | | $12J_g^{3/2}$ | −7.158 |
| | | | $22J_g^{1/2}$ | −7.119 |

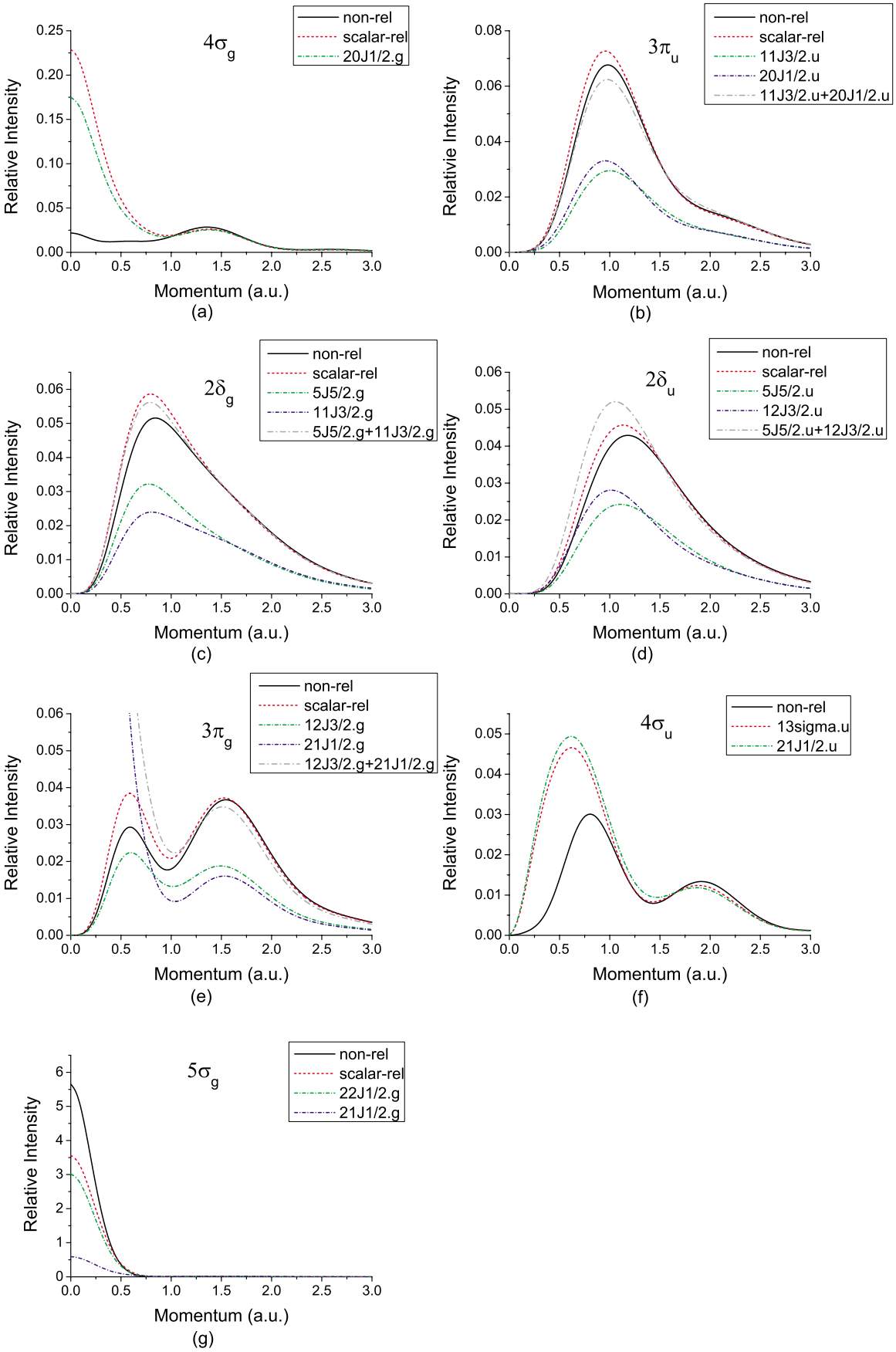


FIG. 6. (Color online) The spherically averaged momentum profiles for valence orbitals of $Au_2$.

fore, the intensity of $21J_g^{1/2}$ in low-momentum region ($p<0.5$ a.u.) is far stronger than that of $3\pi_g$ in Fig. 6(e) and weaker than that of $5\sigma_g$ in Fig. 6(g).

The expansion of the $4\sigma_g$, $3\pi_u$, $2\delta_g$, $2\delta_u$, $3\pi_g$, and $4\sigma_u$ orbitals in position space under relativistic condition result from the reasons that these orbitals are formed by $5d$ atomic orbital electron, while $d$ atomic orbitals extend in position space.

The $5\sigma_g$ orbital, whose momentum profile is shown in Fig. 6(g), is the highest occupied molecular orbital (HOMO) of the $Au_2$ molecule. Contrary to the above-mentioned orbitals, the relative intensity for $5\sigma_g$ orbital using nonrelativistic method is stronger than that using scalar relativistic method in the low-momentum region ($p<0.5$ a.u.), which implies that the $5\sigma_g$ orbital shrinks in position space. This result is in agreement with the explanation that the $5\sigma_g$ molecular orbital is composed of the $6s$ atomic orbitals, which shrink in position space under relativistic effects.

## IV. SUMMARY

This paper introduces the scalar relativistic and two-component relativistic theory to analyze of EMS experimental momentum profiles. The relativistic quantum computation can provide more accurate results than nonrelativistic calculations for a molecule containing high-$Z$ atoms. As the energy resolution and collection efficiency of EMS experiments improve, EMS is able of handling large molecules with increasing accuracy. Although the relativistic quantum chemistry succeeded in the calculations for the heavy elements at the end of last century, its application in the interpretation of EMS experimental results is largely limited to the atomic targets. The combination of high level relativistic calculation and the high-resolution EMS experiment provide us a powerful tool for investigating the electronic structures of molecules with high-$Z$ atoms.

Present work investigated the electronic structures and momentum profiles for the valence orbitals of $I_2$ and $Au_2$ using nonrelativistic, scalar relativistic, and spin-orbit relativistic calculations. The comparison between calculations and experimental momentum distributions for Xe $5P$ states verifies the validity of the calculations. From present investigation, we can obtain the following conclusions. The relativistic effects make the valence molecular orbitals expand or shrink in position space along with their component atomic orbitals for the homonuclear diatomic molecules. The notable intensity for $17J_g^{1/2}$ of $I_2$ in the low-momentum region $p<0.25$ a.u. is predicted using spin-orbit relativistic calculations, which does not exist in the nonrelativistic calculations. We have tried to measure the $I_2$ sample with our spectrometer. However, it was found that there were discernible changes on the polish surface of some copper and steel parts in our spectrometer due to the exposition in the $I_2$ vapor. It would be worthy further EMS measurements on the $I_2$ with improvement of anticorrosion technique to test this result. $Au_2$ molecule exhibits very strong relativistic effects with the large shift of binding energy and the complicated split of spin-orbit coupling. The huge difference between the relativistic calculations and nonrelativistic calculations for its valence molecular-orbital momentum profiles is found. In conclusion, the relativistic quantum-chemistry theory is an indispensable tool for the accurate analysis of EMS results of molecules containing high-$Z$ atoms.

## ACKNOWLEDGMENTS

This work was supported by the National Natural Science Foundation of China under Contracts No. 10874097, No. 10704046, and No. 10575062, and Specialized Research Fund for the Doctoral Program of Higher Education under Grant No. 20070003146.

[1] P. A. M. Dirac, Proc. R. Soc. London, Ser. A **123**, 714 (1929).
[2] M. Reiher and B. Hess, in *Modern Methods and Algorithms of Quantum Chemistry*, edited by J. Grotendorst (Jülich Research Center, Jülich, 2000), pp. 451.
[3] P. Pyykkö and J. P. Desclaux, Acc. Chem. Res. **12**, 276 (1979).
[4] P. Pyykkö, Chem. Rev. **88**, 563 (1988).
[5] M. Pepper and B. E. Bursten, Chem. Rev. **91**, 719 (1991).
[6] W. Kutzelnigg, Chem. Phys. **225**, 203 (1997).
[7] W. J. Liu and M. Dolg, Phys. Rev. A **57**, 1721 (1998).
[8] W. J. Liu, M. Dolg, and L. M. Li, J. Chem. Phys. **108**, 2886 (1998).
[9] G. te Velde *et al.*, J. Comput. Chem. **22**, 931 (2001).
[10] W. J. Liu, F. Wang, and L. M. Li, J. Theor. Comput. Chem. **2**, 257 (2003).
[11] I. E. McCarthy and E. Weigold, Rep. Prog. Phys. **54**, 789 (1991).
[12] M. A. Coplan, J. H. Moore, and J. P. Doering, Rev. Mod. Phys. **66**, 985 (1994).
[13] E. Weigold and I. E. McCarthy, *Electron Momentum Spectroscopy* (Kluwer Academic/Plenum, New York, 1999).
[14] J. P. D. Cook, J. Mitroy, and E. Weigold, Phys. Rev. Lett. **52**, 1116 (1984).
[15] J. P. D. Cook, I. E. McCarthy, J. Mitroy, and E. Weigold, Phys. Rev. A **33**, 211 (1986).
[16] L. Frost, J. Mitroy, and E. Weigold, J. Phys. B **19**, 4063 (1986).
[17] J. Bonfert, H. Graf, and W. Nakel, J. Phys. B **24**, 1423 (1991).
[18] X. G. Ren, C. G. Ning, J. K. Deng, G. L. Su, S. F. Zhang, and Y. R. Huang, Phys. Rev. A **73**, 042714 (2006).
[19] Z. Li *et al.*, Chem. Phys. Lett. **457**, 45 (2008).
[20] C. G. Ning *et al.*, Chem. Phys. **343**, 19 (2008).
[21] P. Duffy, D. P. Chong, M. E. Casida, and D. R. Salahub, Phys. Rev. A **50**, 4707 (1994).
[22] X. G. Ren *et al.*, Rev. Sci. Instrum. **76**, 063103 (2005).
[23] C. Lee, W. Yang, and R. G. Parr, Phys. Rev. B **37**, 785 (1988).
[24] C. F. Guerra *et al.*, Theor. Chem. Acc. **99**, 391 (1998).
[25] E. J. Baerends *et al.*, *ADF* (SCM, Amsterdam, 2008).
[26] E. van Lenthe, E. J. Baerends, and J. G. Snijders, J. Chem. Phys. **101**, 9783 (1994).
[27] L. Visscher, Chem. Phys. Lett. **253**, 20 (1996).

[28] P. Pyykkö and H. Toivonen, *Tables of Representation and Rotation Matrices for the Relativistic Irreducible Representations of 38 Point Groups* (Abo Akademi, Abo, 1983), Vol. 43.
[29] A. B. Cornford *et al.*, J. Chem. Phys. **54**, 2651 (1971).
[30] A. W. Potts and W. C. Price, Trans. Faraday Soc. **67**, 1242 (1971).
[31] B. R. Higginson, D. R. Lloyd, and P. J. Roberts, Chem. Phys. Lett. **19**, 480 (1973).
[32] S. Hamel *et al.*, J. Electron Spectrosc. Relat. Phenom. **123**, 345 (2002).